Available online at www.sciencedirect.com
SCIENCE DIRECT
Journal of Magnetic Resonance 178 (2006) 237–247
JMR Journal of Magnetic Resonance
www.elsevier.com/locate/jmr

Measurement of magnetic susceptibility and calculation of shape factor of NMR samples

Roy E. Hoffman *

Department of Organic Chemistry, Hebrew University, Jerusalem 91904, Israel

Received 22 June 2005; revised 5 September 2005
Available online 25 October 2005

Abstract

A method for accurate measurement of magnetic susceptibility and determination of the shape factor in an NMR tube is shown. The combination of accurate shape factor determination with susceptibility measurement leads to improved accuracy when measuring chemical shift. This is important for comparing samples in different solvents or under different conditions, such as temperature, solvent, and pH.

Keywords: Shape factor; Susceptibility; Chemical shift; BMS shift

1. Introduction

The observed shift of an NMR signal is dependent on extra factors, often ignored, in addition to chemical shift. Magnetic susceptibility combined with shape factor—termed the bulk magnetic susceptibility (BMS) shift [1]—affect the observed shift by typically 3 ppm, although, in most cases, the effect only varies between samples by about 1 ppm. Chemical shift pertains to isotropically averaged magnetic effects on the atomic and molecular scale, while BMS shift relates to non-isotropic magnetic effects, that are macroscopic in homogeneous liquids, namely those caused by induced dipoles at the boundaries of the sample [1,2]. Calculations are necessary to elucidate the effects of chemical and BMS shifts that can be verified experimentally [3]. However, the BMS shift is the same for all the signals within one homogeneous sample, so it can safely be ignored when comparing resonances within a single sample. The BMS shift varies very little between dilute samples in the same solvent and of the same shape and so, again it can often be ignored.

The problem arises when comparing samples in different solvents and different experimental conditions. Earlier chemical shift standards [4] relied on the assumption that TMS had the same chemical shift in all solvents. However, this was quickly shown not to be the case [5,6] with the chemical shift of TMS now known to vary by over 1 ppm between solvents [7] and, to a lesser extent, with temperature [8], concentration, and pH [9]. As a result, the current IUPAC chemical shift standard [10] adopted dilute TMS in $CDCl_3$ as the prime standard for ^1H NMR, but does not give clear guidelines regarding other solvents. This standard sets chemical shift references for other nuclei as ratios, Ξ, of the prime standard.

While there are methods to measure magnetic susceptibility with a conventional modern NMR spectrometer, adjustment of the observed shift to yield the chemical shift is strongly dependent on the shape factor in addition to the susceptibility. Calculation of the shape factor in all but the simplest cases is mathematically complex. Hence the shape factor of a sample in an NMR tube is usually assumed to be that of an infinite cylinder, an assumption that can lead to errors in the region of 0.1 ppm. This has serious implications for those who try to determine secondary structure of proteins from their chemical shift [11,12] or try to compare the acidity of protons in different solvent mixtures [13]. Improving the accuracy of the shape factor calculation leads to a more accurate susceptibility measurement.

* Fax: +972 2 6585084.
E-mail address: roy@huji.ac.il.

1090-7807/$ - see front matter © 2005 Elsevier Inc. All rights reserved.
doi:10.1016/j.jmr.2005.09.009

For example, a discrepancy of nearly 0.5 ppm occurs when comparing the chemical shift of chloroform in C_6D_6 with that in $CDCl_3$. The difference is 1.52 ppm due to a component of the chemical shift known as the aromatic solvent induced shift (ASIS) [5] but the observed shift upon exchanging samples is only 1.07 ppm, the discrepancy being due to the BMS shift. Discrepancies of over 3 ppm can be contrived by comparing observed shifts in the vapor phase with those of CH_2I_2 solutions [7].

These unaccounted for discrepancies have made the effect of solvent polarizability difficult to study by ^1H NMR because they are often smaller than the BMS shift. For example, the chemical shift of chloroform changes by 0.58 ppm between $CDCl_3$ and CH_2I_2, but the observed shift changes by only 0.29 ppm [7].

The pH affects the chemical shift of water. For example, the chemical shift of HOD in D_2O is reduced by 0.2 ppm in a 0.1 M NaOD solution. Even the chemical shift standards for aqueous solutions (DSS and TSP) are known to be affected by pH, ionic strength, and protein binding [14,15].

A task group is currently conducting an IUPAC project to extend the recommendations of 2001 [10] to account for effects of solvent, temperature, magnetic susceptibility, and various solid-state effects [16]. This paper addresses some magnetic susceptibility aspects of the project.

2. Calculating the effect of susceptibility

The chemical shift, δ, can be determined for a sample in a tube with negligibly thin walls (Eq. (1), where δ_o is the observed shift, δ_χ is the BMS shift, $\bar{\alpha}$ is the effective average shape factor of the sample and κ is the unit-less volume susceptibility of the sample). To be more precise, the effective shape factor is a combination of the spatial distributions of the shape factor and the coil sensitivity (Eq. (2), where I is the coil sensitivity for the volume element and v is volume). SI units and conventions for susceptibility and shape factor have been used throughout this work. However, most published tables of magnetic susceptibilities (e.g. [17,18]) are in cgs units. To convert from cgs units to SI, the magnetic susceptibility must be multiplied by 4π and the shape factor must be divided by 4π.

$$\delta = \delta_o + \delta_\chi = \delta_o + \left(\frac{1}{3} - \bar{\alpha}\right)\kappa, \tag{1}$$

$$\bar{\alpha} = \frac{\int \alpha I \mathrm{d}v}{\int I \mathrm{d}v}. \tag{2}$$

Previous attempts to measure shape factors empirically [7] are likely flawed because the spectrum required reshimming, thereby modifying the average effective magnetic field, whenever the tube configuration was changed. Therefore, the shape factor must be determined by calculation. If the wall is sufficiently thin, then Eq. (3) (where $\bar{\alpha}_g$ is the effective average shape factor of the outer glass wall and κ_g is the volume susceptibility of Pyrex glass, -11.0 ppm [19]) approximates to Eq. (1) because $\bar{\alpha}_g \to \bar{\alpha}$. The effect of shielding from the probe (κ_p) also changes because the effective probe shape factor, $\bar{\alpha}_p$, is averaged over a different region [19]. Eq. (3) is required when comparing tubes of different shape, or in different positions relative to the receiver coil.

$$\delta = \delta_o + \frac{1}{3} - \bar{\alpha}\kappa - \bar{\alpha}_g\kappa_g - \bar{\alpha}_p\kappa_p. \tag{3}$$

The shape factor for some simple geometric shapes is uniform throughout the sample. For example, 1/3 for a sphere or a cylinder at the magic angle, 0 for an infinite cylinder aligned with the field or 1/2 for an infinite cylinder perpendicular to the field (Table 1) [20].

The shape factor at a point is an integral over the bounding surface of the depth (in the direction of the field) below the point multiplied by the cosine of the angle subtended by the field to the normal to the surface divided by the cube of the distance from the point. It is expressed mathematically as follows (Fig. 1, Eq. (4) where $\alpha(\mathbf{x}_0)$ is the shape factor at point $\mathbf{x}_0$, β is the angle between the

Table 1
Shape factors for selected shapes

Shape in a vertical magnetic field	Shape factor
Infinite vertical cylinder	0
Sphere, infinite cylinder at the magic angle, or anything cylindrically symmetrical about the magic angle[a]	1/3
Infinite horizontal cylinder	1/2
Infinite cylinder at angle φ to the field	$\sin^2\varphi/2$
Infinite sheet	1

[a] The magic angle is $\cos^{-1}\sqrt{1/3} = 54.736°$.

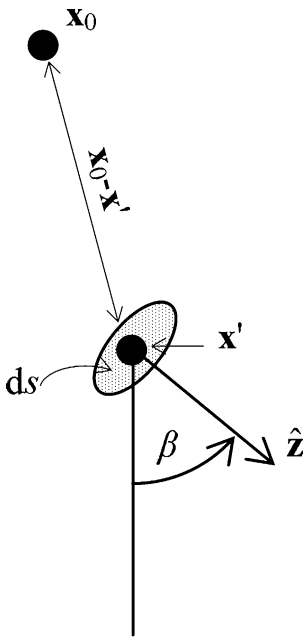

Fig. 1. Calculation of shape factor by integrating over surface elements (Eq. (4), where $\mathbf{x}_0$ is the point for which the shape factor is being calculated, $\mathbf{x}'$ is the location of the surface element, ds is the surface element, $\hat{\mathbf{z}}$ is the unit vector normal to the surface element and β is the angle between the applied magnetic field and the normal to the surface element).

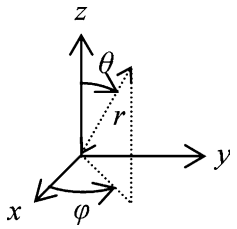

Fig. 2. Spherical coordinates: Cartesian (x,y,z) and polar (r,θ,φ).

normal to the surface element and the field, $\hat{\mathbf{z}}$ is the unit vector normal to the surface element, and s is the surface element) [2,21–24]. (Note that there are errors in [23] that are corrected in [2].)

$$\alpha(\mathbf{x}_0) = \frac{1}{4\pi}\int \cos\beta \frac{[(\mathbf{x}_0 - \mathbf{x}')\cdot\hat{\mathbf{z}}]}{|\mathbf{x}_0 - \mathbf{x}'|^3}\mathrm{d}s. \tag{4}$$

For example, for $\mathbf{x}_0$ at the center of a sphere of radius r, and using spherical coordinates (Fig. 2), where $\mathrm{d}s = r\sin\theta\,\mathrm{d}\theta\, r\,\mathrm{d}\varphi$, one obtains Eq. (5):

$$\begin{aligned}
\alpha(0,0,0) &= -\frac{1}{4\pi}\int_0^{2\pi}\int_0^{\pi}\cos\theta\frac{-r\cos\theta}{r^3}r\sin\theta\,\mathrm{d}\theta\, r\mathrm{d}\varphi,\\
\alpha(0,0,0) &= \frac{1}{4\pi}\int_0^{2\pi}\int_0^{\pi}\cos^2\theta\sin\theta\,\mathrm{d}\theta\,\mathrm{d}\varphi,\\
\alpha(0,0,0) &= -\frac{1}{4\pi}\int_0^{2\pi}\left[\frac{\cos^3\theta}{3}\right]_0^{\pi}\mathrm{d}\varphi,\\
\alpha(0,0,0) &= \frac{1}{4\pi}\int_0^{2\pi}\frac{2}{3}\,\mathrm{d}\varphi,\\
\alpha(0,0,0) &= \frac{1}{3}.
\end{aligned} \tag{5}$$

In the case of a sphere, the integration lends itself to an analytical solution. However, more complex shapes usually require numerical integration. Numerical integration of a sphere shows that for an angular resolution in θ and φ of Δ (in radians), the error is approximately $0.006\Delta^{0.75}$ for $\Delta < 0.1$. For example, to yield an accuracy of 0.0001 in shape factor, the resolution must be 0.004 (over a million elements), and for an accuracy of 0.00001, the resolution must be 0.0002 (nearly 500 million elements).

Scaling the integration steps to the inverse of the integral element reduces the computation time by 38% without reducing accuracy, provided that a maximum step size is set. This maximum step size is optimal at a quarter of the root of the nominal range divided by the nominal step. While this time-saving is not large for a sphere, it is more significant for other shapes.

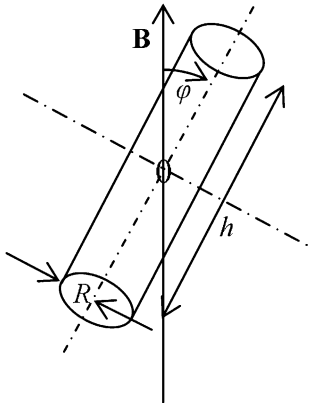

Fig. 3. Finite cylinder of height h and radius R at an angle φ to the field.

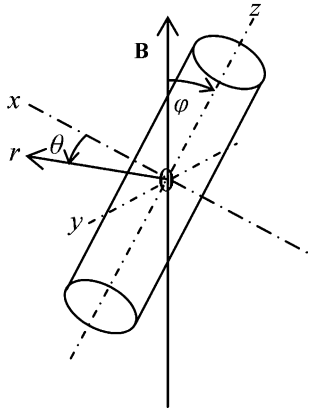

Fig. 4. Tilted cylindrical coordinates (r,θ,z).

For a sphere where the reference point is not at the center, the result is the same but the result is best evaluated numerically (Eq. (6)):

$$\begin{aligned}
\alpha(x,y,z) &= -\frac{1}{4\pi}\int_0^{2\pi}\int_0^{\pi}\cos\theta\frac{z - r\cos\theta}{[(z - r\cos\theta)^2 + (x - r\sin\theta\cos\varphi)^2 + (y - r\sin\theta\sin\varphi)^2]^{3/2}}r\sin\theta\,\mathrm{d}\theta\, r\mathrm{d}\varphi,\\
\alpha(x,y,z) &= \frac{1}{4\pi}\int_0^{2\pi}\int_0^{\pi}\frac{r^2\sin\theta\cos\theta(r\cos\theta - z)}{[(z - r\cos\theta)^2 + (x - r\sin\theta\cos\varphi)^2 + (y - r\sin\theta\sin\varphi)^2]^{3/2}}\mathrm{d}\theta\,\mathrm{d}\varphi,\\
\alpha(x,y,z) &= \frac{1}{4\pi}\int_0^{2\pi}\int_0^{\pi}\frac{r^2\sin\theta\cos\theta(r\cos\theta - z)}{\{r^2 + x^2 + y^2 + z^2 - 2r[z\cos\theta + \sin\theta(x\cos\varphi + y\sin\varphi)]\}^{3/2}}\mathrm{d}\theta\,\mathrm{d}\varphi.
\end{aligned} \tag{6}$$

For a flat-ended, finite cylinder of height h and radius R, tilted at an angle φ to the magnetic field, consider the shape factor for a point at the center (Fig. 3) using tilted cylindrical coordinates (Fig. 4). Here, $\mathrm{d}s = \mathrm{d}r\, r\,\mathrm{d}\theta$ for the ends, and

$ds = R\,dz\,d\theta$ for the wall. For point $\mathbf{x}_0 = (x,\ y,\ z)$ Cartesian $\equiv (r\cos\theta, r\sin\theta, z)$ cylindrical, its dot product with the unit magnetic field vector is given by Eq. (7) in Cartesian coordinates and Eq. (8) in cylindrical coordinates (substituting x with $r\cos\theta$):

$$\mathbf{x}_0 \cdot \hat{\mathbf{B}} = (x,y,z)\cdot(\sin\varphi, 0, \cos\varphi) = z\cos\varphi + x\sin\varphi, \tag{7}$$

$$\mathbf{x}_0 \cdot \hat{\mathbf{B}} = z\cos\varphi + r\cos\theta\sin\varphi. \tag{8}$$

The ends are at $\mathbf{x}' = (r,\theta,\pm\frac{h}{2}) \equiv (r\cos\theta, r\sin\theta, \pm\frac{h}{2})$, and the dot product of their distance from $\mathbf{x}_0$ with the unit magnetic vector is given by Eq. (9)

$$\begin{aligned}(\mathbf{x}_0 - \mathbf{x}')\cdot\hat{\mathbf{B}} &= \left[(x,y,z) - \left(r\cos\theta, r\sin\theta, \pm\frac{h}{2}\right)\right] \\ &\quad\cdot(\pm\sin\varphi, 0, \pm\cos\varphi) \\ &= \pm\left[\left(z \mp \frac{h}{2}\right)\cos\varphi + x\sin\varphi - r\cos\theta\sin\varphi\right].\end{aligned} \tag{9}$$

The distance from $\mathbf{x}_0$ to the ends is given by Eq. (10)

$$\begin{aligned}|\mathbf{x}_0 - \mathbf{x}'| &= \left|(x,y,z) - \left(r\cos\theta, r\sin\theta, \pm\frac{h}{2}\right)\right| \\ &= \sqrt{(r\cos\theta - x)^2 + (r\sin\theta - y)^2 + \left(\pm\frac{h}{2} - z\right)^2} \\ &= \sqrt{r^2\cos^2\theta - 2rx\cos\theta + x^2 + r^2\sin^2\theta - 2ry\sin\theta + y^2 + \left(\frac{h}{2}\mp z\right)^2} \\ &= \sqrt{r^2 + x^2 + y^2 - 2r(x\cos\theta + y\sin\theta) + \left(\frac{h}{2}\mp z\right)^2}.\end{aligned} \tag{10}$$

The wall is at $r = R$ and the dot product of its distance from $\mathbf{x}_0$ with the unit magnetic vector is given by Eq. (11).

$$\begin{aligned}|\mathbf{x}_0 - \mathbf{x}'|\cdot\hat{\mathbf{B}} &= [(x,y,z) - (R\cos\theta, R\sin\theta, Z)] \\ &\quad\cdot(\sin\varphi, 0, \cos\varphi) \\ &= (z - Z)\cos\varphi + x\sin\varphi - R\cos\theta\sin\varphi.\end{aligned} \tag{11}$$

The distance from $\mathbf{x}_0$ to the wall is given by Eq. (12)

$$\begin{aligned}&|(x,y,z) - (R\cos\theta, R\sin\theta, Z)| \\ &= \sqrt{(R\cos\theta - x)^2 + (R\sin\theta - y)^2 + (Z - z)^2} \\ &= \sqrt{R^2\cos^2\theta - 2Rx\cos\theta + x^2 + R^2\sin^2\theta - 2Ry\sin\theta + y^2 + (Z - z)^2} \\ &= \sqrt{R^2 + x^2 + y^2 - 2R(x\cos\theta + y\sin\theta) + (Z - z)^2}.\end{aligned} \tag{12}$$

Combining Eqs. (4), (9)–(12), the shape factor is determined for any point in a tilted finite cylinder (Eq. (13)). Eq. (13) is best evaluated numerically.

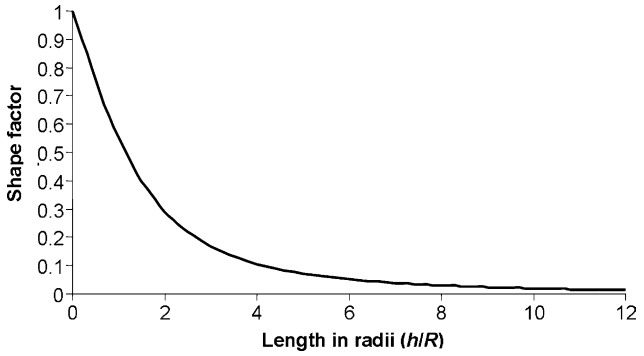

Fig. 5. Graph of shape factor for a vertical cylinder vs. length in radii (h/R).

$$\begin{aligned}&\alpha(x,y,z) \\ &= -\frac{1}{4\pi}\int_0^{2\pi}\int_0^R \left(\frac{\left[\left(z - \frac{h}{2}\right)\cos\varphi + x\sin\varphi - r\sin\varphi\cos\theta\right]}{\left[r^2 + x^2 + y^2 - 2r(x\cos\theta + y\sin\theta) + \left(z - \frac{h}{2}\right)^2\right]^{3/2}}\right. \\ &\quad\left. - \frac{\left[\left(z + \frac{h}{2}\right)\cos\varphi + x\sin\varphi - r\sin\varphi\cos\theta\right]}{\left[r^2 + x^2 + y^2 - 2r(x\cos\theta + y\sin\theta) + \left(z + \frac{h}{2}\right)^2\right]^{3/2}}\right) r\cos\varphi\,dr \\ &\quad + \int_{-\frac{h}{2}}^{\frac{h}{2}} \frac{R\sin\varphi\cos\theta[(z - Z)\cos\varphi + x\sin\varphi - R\sin\varphi\cos\theta]}{[R^2 + x^2 + y^2 - 2R(x\cos\theta + y\sin\theta) + (Z - z)^2]^{3/2}}\,dZ\,d\theta \\ &= \frac{1}{4\pi}\int_0^{2\pi}\int_0^R \left(\sum_{t=0}^{1}(-1)^{t+1}\frac{\left[\left(z - (-1)^t\frac{h}{2}\right)\cos\varphi + x\sin\varphi - r\sin\varphi\cos\theta\right]}{\left[r^2 + x^2 + y^2 - 2r(x\cos\theta + y\sin\theta) + \left(z - (-1)^t\frac{h}{2}\right)^2\right]^{3/2}}\right) \\ &\quad\times r\cos\varphi\,dr + \frac{1}{4\pi}\int_{-\frac{h}{2}}^{\frac{h}{2}} \frac{R\sin\varphi\cos\theta[(z - Z)\cos\varphi + x\sin\varphi - R\sin\varphi\cos\theta]}{[R^2 + x^2 + y^2 - 2R(x\cos\theta + y\sin\theta) + (z - Z)^2]^{3/2}}\,dZ\,d\theta\end{aligned} \tag{13}$$

While Eq. (13) does not lend itself to an analytical solution, special cases of it do and are good for testing any numerical algorithm that implements Eq. (13). The expression for the shape factor at the center of a vertical cylinder can be evaluated analytically (Eq. (16), Fig. 5). As the cylinder length tends to infinity the shape factor tends to zero, and as the cylinder length tends to zero the shape factor tends to that of an infinite sheet, 1. For a cylinder approximating the shape of a typical NMR sample ($R = 2.095$ mm, $h = 39$ mm) the shape factor at the center is 0.00572.

$$\begin{aligned}\alpha(0,0,0) &= \frac{1}{4\pi}\int_0^{2\pi}\int_0^R \left(\sum\nolimits_{t=0}^{1}(-1)^t\frac{-(-1)^t\frac{h}{2}}{\left[r^2 + \left(\frac{h}{2}\right)^2\right]^{3/2}}\right) r\,dr\,d\theta \\ &= \frac{1}{4\pi}\int_0^{2\pi}\int_0^R \frac{rh}{\left[r^2 + \left(\frac{h}{2}\right)^2\right]^{3/2}}\,dr\,d\theta \\ &= \frac{1}{4\pi}\int_0^{2\pi}\left[\frac{-h}{\sqrt{r^2 + \left(\frac{h}{2}\right)^2}}\right]_0^R d\theta \\ &= \frac{1}{4\pi}\int_0^{2\pi}\frac{2h}{h} - \frac{2h}{\sqrt{4R^2 + h^2}}\,d\theta \\ &= \frac{1}{2\pi}\int_0^{2\pi} 1 - \frac{h}{\sqrt{4R^2 + h^2}}\,d\theta = 1 - \frac{h}{\sqrt{4R^2 + h^2}}.\end{aligned} \tag{14}$$

However, for a finite cylinder, the shape factor varies with position. Simplifying Eq. (13) for a vertical cylinder at a point along the center axis yields Eq. (15). At the center of a long cylinder, the shape factor is close to zero and rises to 1/2 at the ends. For a horizontal cylinder, the shape factor is close to 1/2 at the center and falls to 1/4 at the ends.

$$\begin{aligned}\alpha(0,0,z) &= \frac{1}{4\pi}\int_0^{2\pi}\int_0^{R}\left(\sum_{t=0}^{1}(-1)^{t}\frac{z-(-1)^{t}\frac{h}{2}}{\left[r^2+\left(z-(-1)^{t}\frac{h}{2}\right)^2\right]^{3/2}}\right)r\,\mathrm{d}r\,\mathrm{d}\theta\\ &= \frac{1}{4\pi}\int_0^{2\pi}\left[\sum_{t=0}^{1}(-1)^{t}\frac{\frac{h}{2}-(-1)^{t}z}{\sqrt{r^2+\left(z-(-1)^{t}\frac{h}{2}\right)^2}}\right]_0^{R}\mathrm{d}\theta\\ &= \frac{1}{4\pi}\int_0^{2\pi}\sum_{t=0}^{1}(-1)^{t}\left((-1)^{t}\frac{z-(-1)^{t}\frac{h}{2}}{z-(-1)^{t}\frac{h}{2}}-\frac{\frac{h}{2}-(-1)^{t}z}{\sqrt{R^2+\left(z-(-1)^{t}\frac{h}{2}\right)^2}}\right)\mathrm{d}\theta\\ &= \frac{1}{4\pi}\int_0^{2\pi}2-\sum_{t=0}^{1}(-1)^{t}\frac{h-(-1)^{t}2z}{\sqrt{4R^2+(2z-(-1)^{t}h)^2}}\mathrm{d}\theta\\ &= \frac{1}{2}\left(2-\sum_{t=0}^{1}(-1)^{t}\frac{h-(-1)^{t}2z}{\sqrt{4R^2+(2z-(-1)^{t}h)^2}}\right)\\ &= \frac{1}{2}\left(2-\frac{h-2z}{\sqrt{4R^2+(2z-h)^2}}+\frac{h+2z}{\sqrt{4R^2+(2z+h)^2}}\right).\end{aligned}\tag{15}$$

Scaling the numerical integration to the angle subtended allows a large saving in computer time for a long cylinder. The scaling should be limited to a factor of 10 in order to maintain accuracy.

For an NMR tube aligned with the field, the vertical walls contribute nothing to the shape factor. The two remaining contributions are from the bottom and top of the sample. The shape of a sample in a standard NMR tube is a cylinder

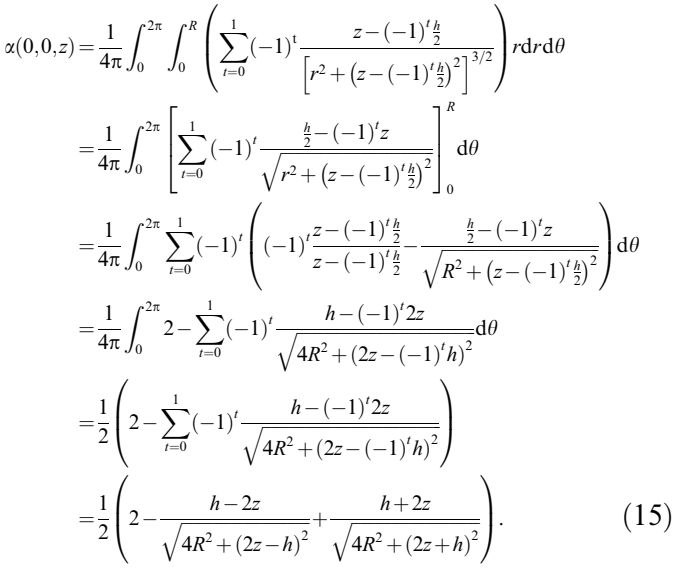

radius (r_2, Fig. 6) of 2.095 mm with a hemispherical bottom (Eq. (16), (17)), and the meniscus at the top approximates to a spherical cap with a depth d_1 of approximately 1.35 mm. The true form of the meniscus is not a spherical cap but the approximation is more than sufficient for its use here. The cylinder walls do not contribute to the shape factor because $\cos\beta$ equals zero. The outer radius of the tube, r_3, is 2.475 mm. The average radius of curvature of the meniscus, r_1, is given by Eqs. (18)–(20) (Fig. 7). $\mathrm{Cos}\,\psi$ is evaluated for both triangles and resolved to give r_1. The shape factors within a flat-ended cylinder and an NMR tube are compared in Fig. 8 and are shown in relation to the coil response curve that is discussed later. The coil response curve indicates the weighting at each position.

The inside bottom is at h

$$= r_3 - d - \sqrt{(r_2^2 - r^2)}, \quad 0 < r < r_2. \tag{16}$$

The outside bottom is at h

$$= r_3 - d - \sqrt{(r_3^2 - r^2)}, \quad 0 < r < r_2, \tag{17}$$

$$\cos\psi = \sqrt{(r_2^2 + d_1^2)}/2r_1 = d_1/\sqrt{(r_2^2 + d_1^2)}, \tag{18}$$

$$r_1 = (r_2^2 + d_1^2)/2d_1. \tag{19}$$

The meniscus is at

$$h = r_1 + l - d - \sqrt{(r_1^2 - r^2)}, \quad 0 < r < r_2. \tag{20}$$

The shape factor for the NMR tube is effectively reduced to the sum of the effects of a hemisphere and a spherical cap. Combining Eqs. (4), (5), (and), (17)–(20) above, we derive the shape factor for an NMR tube to be Eq. (21). The algorithm can be speeded up for axial points ($x = y = 0$), as the φ dependent terms are zero and the integral of each slice with φ can be integrated analytically (Eq. (22)). For off-axis points, the integral has a plane of symmetry, so only a semicircle needs to be integrated (Eq. (23)), speeding up the computation by a factor of two.

$$\begin{aligned}\alpha(x,y,z) = {} & \frac{1}{4\pi}\int_0^{2\pi}\int_{\pi/2}^{\pi}\frac{r_2^2\sin\theta\cos\theta(r_2\cos\theta - z - d + r_3)}{\left\{r_2^2 + x^2 + y^2 + (z+d-r_3)^2 - 2r_2[\cos\theta(z+d-r_3) + \sin\theta(x\cos\varphi + y\sin\varphi)]\right\}^{3/2}}\mathrm{d}\theta\\ & - \int_{\pi-\psi}^{\pi}\frac{r_1^2\sin\theta\cos\theta(r_1\cos\theta - z + l - d + r_1)}{\left\{r_1^2 + x^2 + y^2 + (z-l+d-r_1)^2 - 2r_1[\cos\theta(z-l+d-r_1) + \sin\theta(x\cos\varphi + y\sin\varphi)]\right\}^{3/2}}\mathrm{d}\theta\,\mathrm{d}\varphi,\end{aligned}\tag{21}$$

$$\alpha(0,0,z) = \frac{1}{2}\left\{\int_{\pi/2}^{\pi}\frac{r_2^2\sin\theta\cos\theta(r_2\cos\theta - z - d + r_3)}{[r_2^2 + (z+d-r_3)^2 - 2r_2\cos\theta(z+d-r_3)]^{3/2}}\mathrm{d}\theta - \int_{\pi-\psi}^{\pi}\frac{r_1^2\sin\theta\cos\theta(r_1\cos\theta - z + l - d + r_1)}{[r_1^2 + (z-l+d-r_1)^2 - 2r_1]^{3/2}}\mathrm{d}\theta\right\},\tag{22}$$

$$\begin{aligned}\alpha(x,y,z) = {} & \frac{1}{2\pi}\int_{\tan^{-1}\left(\frac{y}{x}\right)}^{\pi+\tan^{-1}\left(\frac{y}{x}\right)}\int_{\pi/2}^{\pi}\frac{r_2^2\sin\theta\cos\theta(r_2\cos\theta - z - d + r_3)}{\{r_2^2 + x^2 + y^2 + (z+d-r_3)^2 - 2r_2[\cos\theta(z+d-r_3) + \sin\theta(x\cos\varphi + y\sin\varphi)]\}^{3/2}}\mathrm{d}\theta\\ & - \int_{\pi-\psi}^{\pi}\frac{r_1^2\sin\theta\cos\theta(r_1\cos\theta - z + l - d + r_1)}{\{r_1^2 + x^2 + y^2 + (z-l+d-r_1)^2 - 2r_1[\cos\theta(z-l+d-r_1) + \sin\theta(x\cos\varphi + y\sin\varphi)]\}^{3/2}}\mathrm{d}\theta\,\mathrm{d}\varphi.\end{aligned}\tag{23}$$

For example, an NMR sample of dimensions $l = 40$ mm and $d = 20$ mm could be approximated to a cylinder 39.46 mm long offset upwards from the center by 0.56 mm, and would yield a shape factor at the origin of

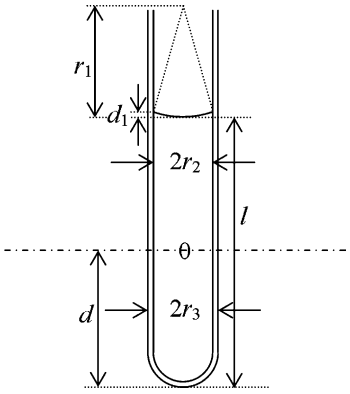

Fig. 6. NMR sample where d is the depth of the outer bottom of the tube below the coil center, d_1 is the depth of the meniscus, l is the liquid depth, r_1 approximates the meniscus' radius of curvature, r_2 is the inner radius of the tube, and r_3 is the outer radius of the tube.

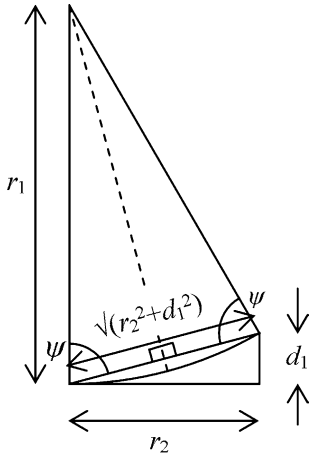

Fig. 7. Approximation of the meniscus shape to a spherical cap, where ψ is 90° minus half the angle subtended by the spherical cap and the other symbols are as in Fig. 6.

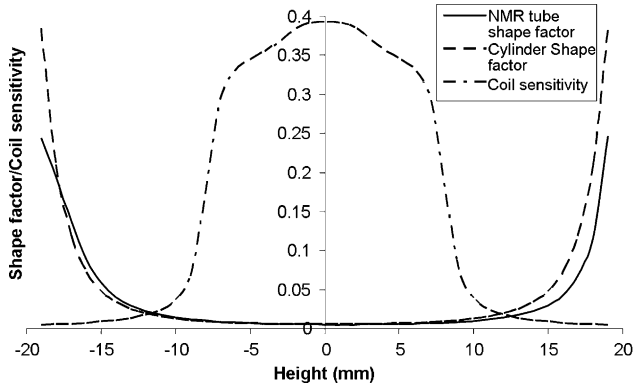

Fig. 8. Shape factor and coil response versus position for a 39 mm long cylinder of radius 2.095 mm (typical of a 5 mm NMR sample).

0.00560, while the shape factor calculated taking into account the curvature of the ends is 0.00526, a difference of 0.00034.

The effective shape factor is dependent on the excitation profile of the probe (Eq. (2)). In a Bruker DRX 400 spectrometer with a BBI 5 mm z-grad probe (used in this work) and similar instruments, the excitation profile of a saddle coil in the probe may approximate to a rectangle, a convolution product of a rectangular function with a Lorentzian (Eq. (24)) or with a Gaussian (Eq. (25)).

Lorentzian

$$\begin{aligned} a(|x|<c) * \frac{b}{1+b^2x^2/2} &= \int_{-c}^{c} \frac{ab}{1+b^2(x-t)^2/2}\mathrm{d}t \\ &= \int_{-c}^{c} \frac{ab}{1+b^2x^2/2-b^2xt+b^2t^2/2}\mathrm{d}t \\ &= \left[a\tan^{-1}\left(\frac{b^2t-b^2x}{b}\right)\right]_{-c}^{c} \\ &= \left[a\tan^{-1}[b(t-x)]\right]_{-c}^{c} \\ &= a\{\tan^{-1}[b(c-x)]+\tan^{-1}[b(c+x)]\}. \end{aligned} \tag{24}$$

Gaussian

$$\begin{aligned} a(|x|<c) * \frac{2}{\sqrt{\pi}}\exp(-b^2x^2) &= \frac{2a}{\sqrt{\pi}}\int_{-c}^{c}\exp[-b^2(x-t)^2]\mathrm{d}t \\ &= a\{erf[b(x-c)]-erf[b(x+c)]\}. \end{aligned} \tag{25}$$

The Lorentzian convolution fits the profile, measured by obtaining the spectrum with an applied field gradient, better than the Gaussian profile. However, the probe contains two coils that interact, and it transpires that a sum of two Lorentzian (Eq. (26)), where a is the height of the response, b is rounding of the edges and c is the half width of the response or two Gaussian (Eq. (27)) convolutions fit the observed data much better than one, and the best fit is obtained for the double Lorentzian convolution (Eq. (26)):

$$\begin{aligned} I = {} & a_1\{\tan^{-1}[b_1(c_1-x)]+\tan^{-1}[b_1(c_1+x)]\} \\ & + a_2\{\tan^{-1}[b_2(c_2-x)]+\tan^{-1}[b_2(c_2+x)]\}, \end{aligned} \tag{26}$$

$$\begin{aligned} I = {} & a_1\{\mathrm{erf}[b_1(x-c_1)]-\mathrm{erf}[b_1(x+c_1)]\} \\ & + a_2\{\mathrm{erf}[b_2(x-c_2)]-\mathrm{erf}[b_2(x+c_2)]\}. \end{aligned} \tag{27}$$

The excitation profile for a 5 mm BBI probe fits the function with the tabulated parameters (Table 2, Fig. 9). The mean shape factor is the integral of the product of shape factor and excitation profile intensity for each point in the sample divided by the integration of the excitation profile. Table 3 compares the shape factor at the center of the sample with the different excitation profile models and compares integration (Eq. (2)) along the central axis of the sample (Eq. (28)) with integration of the full volume of the sample (Eq. (29)). The effective shape factors for NMR tubes of various depths and liquid heights are shown in Fig. 10. However, it was found that the result was less sensitive to the coarseness of the integration over the profile by a factor of nine in each dimension as compared to

Table 2
Models for excitation profile of 400 MHz 5 mm BBI z-grad probe

Coil	a_1	a_2	b_1	b_2	c_1	c_2	Offset
Rectangular					8.19		
Inner Lorentzian	3.01	0.35	1.36	1.26	8.19	3.09	−0.10
Inner Gaussian	2.78	0.47	0.41	0.31	8.41	4.74	−0.06
Outer Lorentzian	2.66	0.77	0.86	1.14	7.28	4.04	−0.14

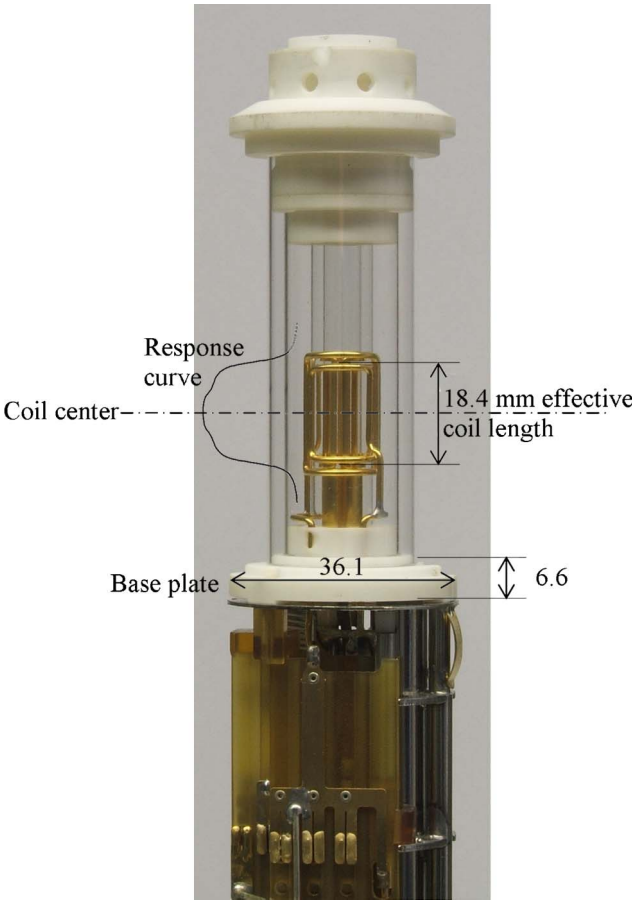

Fig. 9. Inside a Bruker BBI probe-head showing the response curve for the inner coils.

the coarseness of integration over the surface. This allows a saving of nearly two orders of magnitude in computing time and yields results comparable to those in Table 3:

$$\bar{\alpha} = \frac{\int \alpha I \, dz}{\int I \, dz}, \tag{28}$$

$$\bar{\alpha} = \frac{2\pi \int\int \alpha I r \, dr \, dz}{2\pi \int\int I r dr \, dz}. \tag{29}$$

3. Application to magnetic susceptibility measurement

In the past, magnetic susceptibility has been measured using a magnetic susceptibility balance [25] or by NMR using a horizontally aligned electromagnet [26,27]. The magnetic susceptibility balance may be more accurate than some NMR methods, but requires extra instrumentation and careful measurement.

Because horizontally aligned magnets are no longer commonly available, two methods have been proposed for measuring magnetic susceptibility with a vertically aligned magnet.

In the capillary sphere method [26], a glass sphere attached to a capillary containing the sample is immersed in a solvent such as benzene [28]. The sample gives rise to two signals whose separation is proportional to its magnetic susceptibility. Theoretically, the difference in shape factor should be 1/3. However, the shape factor was measured to be between 0.34 and 0.38 [28] so each capillary sphere has to be individually calibrated. Since the uncertainty in shape factor is reported to be at least 0.02 and the uncertainty in susceptibility is approximately 0.1 ppm.

An alternative is to measure the gross distortion of the line-shape caused by raising an NMR tube bottom from 20 mm below the coil center to 2 mm below. Again, each tube must be calibrated but, with care, an accuracy of 0.1 ppm in susceptibility was reported as achievable [7].

For a finite cylinder at the magic angle, the shape factor at the center is 1/3 and the BMS shift is zero. This holds for the point along the central axis of any cylindrically symmetrical object aligned with the magic angle.

Numerical integration shows that for any object cylindrically symmetrical about the magic angle with a cylindrically symmetrical response, each section perpendicular to the magic angle has an average shape factor of 1/3, and hence the effect of susceptibility averages to zero. The sample should be spun to cancel out spatial broadening effects. The result is that the chemical shift can be measured directly [29]. While it has been suggested that BMS shifts are observed with magic angle spinning [30], this has been shown not to be the case [3]. However, small errors in the magic angle lead to large changes in resonant frequency. Setting errors of over 0.1° would significantly degrade routine MAS measurements [31,32], so it can be reasonably assumed that the magic angle was accurate to within this.

Table 3
Mean shape factors for an NMR tube with a liquid height of 40 mm above the outer bottom that is 20 mm below the coil center

Point	Axis			Full		
	Rectangular	Bilorenz	Bigauss	Rectangular	Bilorenz	Bigauss
0.00526	0.00708	0.00758	0.00662	0.00699	0.00734	0.00656
Outer		0.00775			0.00752	

The single point and axial integrations were with a resolution of 0.001 (mm and radians), while the full integration was with a resolution of 0.01.

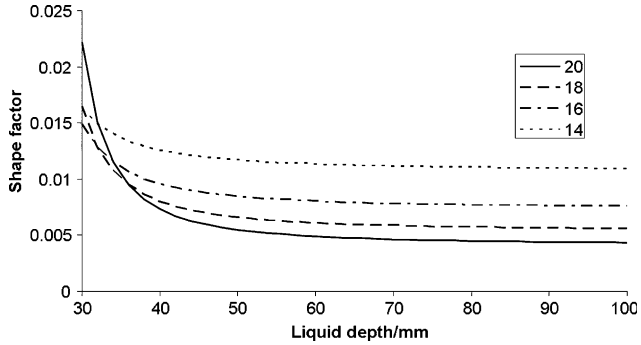

Fig. 10. Shape factors for an NMR tube whose bottom is at various depths (14, 16, 18, and 20 mm) below the coil center.

An error of 0.1° would lead to an error in susceptibility of 0.025 and shift the frequency of water by 0.007 ppm, similar to the accuracy obtainable using an aligned sample and correcting for bulk susceptibility. Therefore, care must be taken in setting the magic angle spinning, in order to make it more accurate than the previous methods [7,27,28,33] mentioned above. However, the magic angle can be measured to within 0.005° and so could be more accurately adjusted, or corrected for yielding an accuracy of 0.0004 ppm.

Some recent deuterium chemical shift measurements [34] at the magic angle (where no susceptibility correction is required) were compared with vertical measurements [8] to calculate the solvent susceptibility from Eq. (30)

$$\kappa = \frac{\Delta\delta_{\text{overtical}} - \Delta\delta_{\text{magic}}}{1/3 - \bar{\alpha}} + \kappa_0. \tag{30}$$

If the samples have different shape factors, then these can be corrected for Eq. (31)

$$\kappa = \frac{\Delta\delta_{\text{overtical}} - \Delta\delta_{\text{magic}} + \left(\frac{1}{3} - \bar{\alpha}_0\right)\kappa_0}{1/3 - \bar{\alpha}}. \tag{31}$$

Here, the known susceptibility for D_2O at 27.3 °C ($\kappa_0 = -8.857$ ppm [17]), is used as a standard. The values of $\Delta\delta$ represent the differences in the observed shift between the solvent and D_2O, as given in Table 4. This method is more accurate than the techniques described previously [7], but measurements from the two methods generally agree. The standard error between the two methods is 0.25 ppm, more than twice the previously estimated error (0.11 ppm) [7]. Given that the expected error in susceptibility for the new method is 0.02 ppm, it is likely that the previous accuracy was underestimated. Of course, the new expected error must also come under suspicion of being underestimated. With improvements in the magic angle measurements, it is likely that the error in susceptibility can be reduced to the extent that it arises mostly from uncertainties in shape factor at the vertical angle.

In principle, greater accuracy could be achieved with an accurately defined shape in the region of the detector coil with reasonable accuracy further away. A regular NMR tube is ideal, as it is precisely defined along its walls and reasonably far away and defined at the ends of the sample. An error in alignment with the magnet has much less effect than at the magic angle: a 0.1° error would shift the water signal by 0.00001 ppm. A similar error of 0.00002 ppm would be caused for an NMR tube perpendicular to the magnetic field. The greatest accuracy in measuring susceptibility and chemical shift can be obtained using two magnets, one horizontal and one vertical. The sample would be compared with a signal of low susceptibility (e.g., TMS vapor) in each magnet. TMS vapor is easily detectable at 0.1 amagats (atmospheres at 0 °C) when its volume susceptibility is -0.00402 ± 0.00009 ppm. The uncertainty in TMS's susceptibility would give rise to an error in the observed shift of 0.00003 ppm. This accuracy would be compromised by the limited accuracy of the shape factor, yielding a practical error limit of about 0.001 ppm.

However, high-resolution horizontal bore instruments are no longer manufactured and would have to be pro-

Table 4
Measurement of susceptibility using magic angle measurements[a]

Solvent	$^{D}\delta$ (magic angle)	$^{D}\delta_o$ (vertical)	Shape factor	κ (ppm)	Molar [b] (vol/cm^3 mol^{-1})	χ_M (ppmcm^{3}mol^{-1})
$CDCl_3$	7.163	4.263	0.00088	−9.149	80.49	−736.4
D_2O	4.641	1.839	0.00105	−8.859	18. 10[c]	−160.3 [d]
Acetone-d_6	1.810	0.069	0.00078	−5.661	74.08	−419.4
CD_3CN	1.837	−0.183	0.00078	−6.500	52.85	−343.5
THF-d_8	1.532 3.391	−0.958 0.900	0.00075	−7.914	81.91	−648.2
CD_3OD	3.119 4.633	0.968 2.495	0.00082	−6.895	40.58	−279.8
DMSO-d_6	2.507	0.075	0.00069	−7.737	71.72	−554.9

[a] At 27.3 °C as determined from the methanol deuterium chemical shift difference [8].
[b] Molar volume (with the exception of D_2O) is derived by combining the expansion rates of the protiated solvent [35] with the density of the deuterated solvent [36] at 25 °C.
[c] Derived from the density of D_2O [17].
[d] Ref. [17].

duced specially for this application. Therefore, the use of the magic angle combined with accurate measurement of the angle is a much more practical and cost-effective solution to achieve the same result.

4. Effect of changing the sample shape and position

The magnetic field inside the sample and hence the resonant frequency is dependent on the shape and susceptibility of the tube and the probe. When exchanging the sample, the probe does not change and no significant change occurs in the tube if the same type of tube is used in the same position. However, it is sometimes necessary to compare samples in different tubes or tubes at different depths. The main effect is at the bottom of the tube (Eq. (32), that can be optimized for computation in the same manner as Eq. (21)). This needs to be integrated over the sample volume (Eqs. (2), (28), and (29)) and before being used to calculate the shielding effect of the tube according to Eq. (33). A standard NMR tube has an effective shape factor of 0.0173, which multiplied by the susceptibility of borosilicate glass (−11 ppm) causes a shielding of 0.015 ppm. Moving the tube up by 10 mm increases the shielding to 0.048 ppm, a difference of 0.033 ppm. The contribution of the cap can be approximated to a cylinder (Eq. (13), where the last term is zero for a vertical tube), but must be considered separately because it is a different material and so has a different susceptibility. Typically the cap has a radius of 4.2 mm, height of 4.7 mm and is centered 160 mm above the coil-center. The cap's effective shape factor is only 0.00001 and has an approximate susceptibility of −8 ppm and so contributes an insignificant shielding of 0.00008 ppm:

$$\begin{aligned}\alpha(x,y,z) = &\int_0^{2\pi}\int_{\pi/2}^{\pi} \frac{r_3^2 \sin\theta\cos\theta(r_2\cos\theta - z - d + r_3)}{\{r_2^2 + x^2 + y^2 + (z+d-r_3)^2 - 2r_2[\cos\theta(z+d-r_3) + \sin\theta(x\cos\varphi + y\sin\varphi)]\}^{3/2}}\,\mathrm{d}\theta \\ &- \int_{\pi/2}^{\pi} \frac{r_3^2 \sin\theta\cos\theta(r_2\cos\theta - z - d + r_3)}{\{r_3^2 + x^2 + y^2 + (z+d-r_3)^2 - 2r_3[\cos\theta(z+d-r_3) + \sin\theta(x\cos\varphi + y\sin\varphi)]\}^{3/2}}\,\mathrm{d}\theta\,\mathrm{d}\varphi, \end{aligned} \tag{32}$$

$$\begin{aligned}\delta &= \delta_o + \frac{\int\left(\frac{\kappa}{3} - \alpha\kappa - \alpha_g\kappa_g\right)I\,\mathrm{d}v}{\int I\,\mathrm{d}v} \\ &= \delta_o + \frac{\kappa}{3} - \frac{\int\left(\alpha\kappa + \alpha_g\kappa_g\right)I\,\mathrm{d}v}{\int I\,\mathrm{d}v}. \end{aligned} \tag{33}$$

The calculated effect can now be applied to real samples. The predicted effect of raising an NMR tube containing an 85 mm deep sample of D_2O from 20 to 10 mm below the center of the BBI probe is 0.231 ppm and was measured to be 0.115 ppm. Likewise for glycol, (56 mm deep with 3% DMSO-d_6) the calculated shift is 0.23 ppm and was measured to be 0.13 ppm. The reduction in the observed shift is probably due to the reduction in shielding at the bottom of the sample arising from the base of the probe when the sample is raised. This shows that the resonant frequency of different shaped samples is dependent on elements of the probe structure. It is noted in the literature that probe performance is critically dependent on the magnetic susceptibility of its components [19]. The probe has a ceramic and metallic platter under the sample. If approximated to a cylinder of 36.1 mm diameter and 6.6 mm height then its mean shape factor changes by 0.0014 on raising the sample 10 mm and most of this change occurs between 13 and 10 mm. The effect of the upper part of the probe is calculated to be approximately five times smaller. However, the much greater observed effect of 0.11 ppm suggests that the metallic structures under the base-plate have a much greater effect. The solution is to calibrate the shielding effect with sample position or to ensure that the shape and position of the sample are identical when comparing different samples. The latter is the more accurate method where possible.

5. Effect of using different coils in a probe

The fact that the inner and outer coils have different response curves suggests that there is a difference in the frequency depending on the coil used for measurement. This puts a limit on the accuracy of about 0.0017 ppm for directly referencing X-nuclei against ^1H (the Ξ method). In principle, this effect could be observed by comparing the frequency as measured directly with that measured by heteronuclear correlation. For example, the ^{13}C signal of TMS has a line-width of 0.2 Hz in $CDCl_3$ and an expected effect of 0.17 Hz. This effect is difficult to observe and measure, and special precautions have to be taken to ensure that physical conditions are as similar as possible for the two experiments [37]. The main problem is ensuring that the sample is at the same temperature during acquisition. CPD-decoupling is precluded because the amount of heating differs between ^1H and ^{13}C decoupling, so the ^{13}C spectrum has to be coupled to ^1H and the heteronuclear correlation has to be coupled to ^{13}C in f_2. The ^{13}C acquisition has to be modified to include a dummy correlation pulse sequence that dumps the same amount of heat into the sample as correlation does. Three minutes of dummy acquisition has to precede each experiment to achieve a thermal steady state. By taking such precautions, shifts of

5% of the line-width can be measured. In practice, for 15% TMS in $CDCl_3$ with a sample height of 61.5 mm, the difference is calculated to be 0.0009 ppm and measured as 0.0006 ppm. This also partially explains the discrepancies as high as 0.002 ppm in Ξ values reported [10] when measured on different spectrometers although slight temperature differences are an alternative explanation. The implications are that for most purposes, the Ξ method is reliable, but it is important to know that its accuracy is limited. Wherever sub-ppb precision is required, inverse detection is necessary.

6. Conclusions

It is shown that there are limitations on the accuracy when comparing chemical shifts of differently shaped samples. Even using different coils in the same probe causes a slight difference in frequency. This puts a limit on the accuracy when comparing frequencies of different nuclei by direct observation using the Ξ scale, although, for most purposes, the difference is negligible.

Methods have been proposed for accurate determination of the shape factor, susceptibility, and hence chemical shift. The combination of accurate shape-factor determination with previously published methods of susceptibility measurement leads to the improved accuracy. The greatest accuracy is expected to be achieved using a combination of two orientations, one horizontal or at the magic angle and one vertical. This will have an impact on the study of the effect of physical conditions such as temperature and solvent and chemical conditions such as pH and protein folding on chemical shift. Accurate magnetic susceptibility measurement opens up another physical property by which chemical effects can be explored.

Acknowledgments

I thank the Margaret Thatcher Center of Interdepartmental Scientific Equipment for NMR facilities. This work was undertaken as part of an IUPAC Project [16]. The results presented here will be submitted to the project task group for inclusion in their report and eventual publication as an IUPAC Recommendation after appropriate review and public comment. Until then, these results should not be considered as having been endorsed by IUPAC. I thank Maurice Cohen, Noach Treitel, and members of the IUPAC task group, especially Edwin Becker and Pierre Granger, for useful discussions.

References

[1] S.C.-K. Chu, Y. Xu, J.A. Balschi, C.S. Springer Jr., Bulk magnetic susceptibility shifts in NMR studies of compartmentalized samples: use of paramagnetic reagents, Magn. Reson. Med. 13 (1990) 239–262.
[2] C.J. Durrant, M.P. Hertzberg, P.W. Kuchel, Magnetic susceptibility: further insights into macroscopic and microscopic fields and the sphere of Lorentz, Conc. Magn. Reson. A 18 (2003) 72–95.
[3] D.J. Philp, W.A. Bubb, P.W. Kuchel, Chemical shift and magnetic susceptibility contributions to the separation of intracellular and supernatant resonances in variable angle spinning NMR spectra of erythrocyte suspensions, Magn. Reson. Med. 51 (2004) 441–444.
[4] Commission on Molecular Structure and Spectroscopy, Recommendations for the presentation of NMR data for publications in chemical journals, Pure Appl. Chem. 29 (1972) 627–628.
[5] F.H.A. Rummens, R.H. Krystynhak, Intermolecular interaction in nuclear magnetic resonance. VII. The role of the internal reference in aromatic solvent induced shifts, J. Am. Chem. Soc. 94 (1972) 6914–6921.
[6] M.R. Bacon, G.E. Maciel, Solvent effects of the five shielding constants in tetramethylsilane and cyclohexane, J. Am. Chem. Soc. 95 (1973) 2413–2426.
[7] R.E. Hoffman, Variations on the chemical shift of TMS, J. Magn. Reson. 163 (2003) 325–331.
[8] R.E. Hoffman, E.D. Becker, Temperature dependence of the ^{1}H chemical shift of tetramethylsilane in chloroform, methanol and dimethylsulfoxide, J. Magn. Reson. 176 (2005) 87–98.
[9] A. DeMarco, pH dependences of internal references, J. Magn. Reson. 26 (1977) 527–528.
[10] R.K. Harris, E.D. Becker, S.M. Cabral de Menezes, R. Goodfellow, P. Granger, NMR nomenclature: nuclear spin properties and conventions for chemical shifts. IUPAC recommendations 2001, Pure Appl. Chem. 73 (2001) 1795–1818.
[11] D.S. Wishart, B.D. Sykes, F.M. Richards, Relationship between nuclear magnetic resonance chemical shift and protein secondary structure, J. Mol. Biol. 222 (1991) 311–333.
[12] D.S. Wishart, B.D. Sykes, F.M. Richards, The chemical shift index: a fast and simple method for the assignment of protein secondary structure through NMR spectroscopy, Biochemistry 31 (1992) 1647–1651.
[13] L. Poulad-Meyer, Extraction studies of the transfer of acidic or basic compounds from aqueous phases into multicomponent organic extracting media, Thesis Hebrew University of Jerusalem, 2001.
[14] Y.-F. Lam, G. Kotowycz, Caution concerning the use of sodium 2,2-dimethyl-2-silapentane-5-sulfonate (DSS) as a reference for protein NMR chemical shift studies, FEBS Lett. 78 (1977) 181–183.
[15] D.S. Wishart, C.G. Bigam, J. Yao, F. Abildgaard, H.J. Dyson, E. Oldfied, J.L. Markley, B.D. Sykes, ^{1}H, ^{13}C and ^{15}N chemical shift referencing in biomolecular NMR, J. Biomol. NMR. 6 (1995) 135–140.
[16] R.K. Harris, E.D. Becker, S.M. Cabral de Menzes, P. Granger, R.E. Hoffman, K. Zilm, NMR chemical shifts: updated conventions, IUPAC Project 2003-006-1-100. Available from: <www.iupac.org>.
[17] R.C. Weast, M.J. Astle (Eds.), Handbook of Chemistry and Physics, 62nd edition. CRC Press, Boca Raton, FL, 1982.
[18] Landolt-Börnstein Zahlenwerte und Funktionen aus Physik Chemie Astronomie Geophysik und Technik, 6th edition, 2 Band, 10 Teil, in: W.R. Angus, J. Favède, J. Hoarau, A. Pacault (Eds.), Magnetic Properties II, Springer-Verlag, Berlin, 1967.
[19] F.D. Doty, G. Entzminger, Y.A. Yang, Magnetism in high-resolution NMR probe design. I: General methods, Conc. Magn. Reson. 10 (1998) 133–156.
[20] E.D. Becker, High Resolution NMR, Academic Press, San Diego, CA, 2000, p. 91.
[21] J.D. Jackson, Classical Electrodynamics, second ed., Wiley, New York, 1975.
[22] D. Craik, Magnetism: Principles and Applications, Wiley, New York, 1995, pp. 418–420.
[23] J. Wolber, A. Cherubini, M.O. Leach, A. Bifone, Hyperpolarized ^{129}Xe NMR as a probe for blood oxygenation, Magn. Reson. Med. 43 (2000) 491–496.
[24] L. Li, Magnetic susceptibility quantification for arbitrarily shaped objects in inhomogeneous fields, Magn. Reson. Med. 46 (2001) 907–916.
[25] L. N. Mulay, in: A. Weissberger, B.W. Rossiter (Eds.), Techniques of Chemistry, Wiley-Interscience, New York, vol. 4, 1972, 431.

[26] R. Engel, D. Halpern, S. Bienenfeld, Determination of magnetic moments in solution by nuclear magnetic resonance spectrometry, Anal. Chem. 45 (1973) 367–369.
[27] J.R. Zimmerman, M.R. Foster, Standardization of N.M.R. high resolution spectra, J. Phys. Chem. 61 (1957) 282–289.
[28] P.W. Kuchel, B.E. Chapman, W.A. Bubb, P.E. Hansen, C.J. Durrant, M.P. Hertzberg, Magnetic susceptibility: solutions, emulsions and cells, Conc. Magn. Reson. A 18 (2003) 56–71.
[29] A.N. Garroway, Magic-angle sample spinning of liquids, J. Magn. Reson. (1982) 168–171.
[30] J.-H. Chen, B.M. Enloe, Y. Xiao, D.G. Cory, S. Singer, Isotropic susceptibility shift under MAS: the origin of split water resonances in ^{1}H MAS NMR spectra of cell suspensions, Magn. Reson. Med. 50 (2003) 515–521.
[31] S.E. Ashbrook, S. Wimperis, SCAM-STMAS: satellite-transition MAS NMR of quadrupolar nuclei with self-compensation for magic-angle misset, J. Magn. Reson. 162 (2003) 402–416.
[32] S.E. Ashbrook, S. Wimperis, High-resolution NMR spectroscopy of quadrupolar nuclei in solids: satellite-transition MAS with self-comensation for magic-angle misset, J. Am. Chem. Soc. 124 (2002) 11602–11603.
[33] K. Frei, H.J. Bernstein, Method for determining magnetic susceptibilities by NMR, J. Chem. Phys. 37 (1962) 1891–1892.
[34] P. Granger, M. Piotto, O. Assémat, M. Bourdonneau, NMR chemical shift measurements revisited: high precision measurements, Conc. Magn. Reson. (submitted).
[35] ''Physical and Thermodynamic Properties of Pure Chemicals.'' American Institute of Chemical Engineers, Design Institute for Physical Properties, 1998–2004. See www.aiche.org for availability on-line and in printed form.
[36] Aldrich catalog 2005.
[37] R.E. Hoffman, N. Treitel, M. Rabinovitz, ^{1}H NMR isotope shifts arising from the substitution of ^{12}C by ^{13}C: application to polycyclic aromatic hydrocarbon anions, Magn. Reson. Chem. 39 (2001) 489–494.